AIAA 2005–0969

Some Extensions to the Aerothermodynamic Performance Study of Flat-Nose Power-Law Bodies

Wilson F. N. Santos

Combustion and Propulsion Laboratory
National Institute for Space Research
Cachoeira Paulista – SP, 12630–000 BRAZIL

43rd AIAA Aerospace Sciences Meeting and Exhibit
January 10–13, 2005/Reno, NV

Some Extensions to the Aerothermodynamic Performance Study of Flat-Nose Power-Law Bodies

Wilson F. N. Santos*
National Institute for Space Research
Cachoeira Paulista, SP 12630–000 BRAZIL

A numerical study is reported on a new family of blunt leading edges, flat-nose power-law leading edges, situated in a rarefied hypersonic flow. The work is motivated by interest in investigating the aerothermodynamic characteristics of these new shapes as possible candidates for blunting geometries of hypersonic leading edges. The sensitivity of the stagnation point heating, total drag and shock wave standoff distance to nose-thickness and afterbody-shape variations of such leading edges is calculated by using the Direct Simulation Monte Carlo (DSMC) method. Comparisons based on equivalent stagnation point heating, equivalent total drag and equivalent shock standoff distance are made between flat-nose power-law shapes and round leading edges, usually assumed as the appropriate blunting geometry for heat transfer considerations. For the flow conditions considered, round leading edges provided lower drag and smaller shock standoff distance than the majority of the flat-nose power-law leading edges for equivalent stagnation point heating. It was also found that flat-nose power-law shapes yielded much smaller shock standoff distance than the round leading edges for equivalent total drag. The analysis also showed that flat-nose power-law shapes performed better than the round leading edges for those cases with nose thickness of the order of the freestream mean free path.

Nomenclature

a	Constant in power-law body equation
C_d	Drag coefficient, $2D/\rho_\infty V_\infty^2 H$
C_f	Skin friction coefficient, $2\tau_w/\rho_\infty V_\infty^2$
C_h	Heat transfer coefficient, $2q_w/\rho_\infty V_\infty^3$
C_p	Pressure coefficient, $2(p_w - p_\infty)/\rho_\infty V_\infty^2$
D	Drag force, N
H	Body height at the base, m
Kn	Knudsen number, λ/l
L	Body length, m
l	Characteristic length, m
M	Mach number
n	Body power law exponent, number density, m^{-3}
p	Pressure, $\mathrm{N/m}^2$
q	Heat flux, $\mathrm{W/m}^2$
R	Circular cylinder radius, m
Re	Reynolds number, $\rho V l/\mu$

*Researcher, Combustion and Propulsion Laboratory. AIAA Member.

s	Arc length, m
T	Temperature, K
t	Leading edge thickness, m
V	Velocity, m/s
x, y	Cartesian axes in physical space, m
y_{nose}	Half thickness of the body nose, m
η	Coordinate normal to body surface, m
θ	Wedge half angle, body slope angle, degree
λ	Mean free path, m
ξ	Coordinate tangent to body surface, m
ρ	Density, kg/m^3
τ	Shear stress, N/m^2

Subscript

cyl	Circular cylinder
o	Stagnation point conditions
pwr	Power law
w	Wall conditions
∞	Freestream conditions

I. Introduction

THE problems related to the aerothermodynamics at high flight Mach numbers have recently received the attention of several investigations because of their importance in connection with hypersonic vehicles and re-entry problems. Hypersonic vehicles are generally characterized by slender bodies and sharp leading edges in order to achieve good aerodynamic properties like high lift and low drag. Nevertheless, at high Mach numbers, the vehicle leading edges should be sufficiently blunt in order to reduce the heat transfer rate to acceptable levels, and possibly to allow for internal heat conduction. In addition, as aerodynamic heating may cause serious problems at these speeds, the removal of heat near the front of the leading edge must be considered, since the stagnation region is one of the most thermally stressed zones. Therefore, designing a hypersonic vehicle leading edge involves a tradeoff between making the leading edge sharp enough to obtain acceptable aerodynamic and propulsion efficiency and blunt enough to reduce the aerodynamic heating in the stagnation point.

Recently, considerable attention has been given to the problem of calculating aerodynamic characteristics of power law bodies ($y \propto x^n, 0 < n < 1$) at hypersonic speed[1−10]. The major interest in these works has gone into considering the power law shapes as possible candidates for blunting geometries of hypersonic leading edges, such as hypersonic waverider vehicles[11] which have been lately considered for high-altitude/low-density applications[12−15]. The interest in power law shape is based on the work of Mason and Lee[16], who have pointed out that, for certain exponents, power law shapes exhibit aerodynamic properties similar to geometrically sharp shapes. They suggested the possibility of a difference between shapes that are geometrically sharp and shapes that behave aerodynamically as if they were sharp.

Of particular significance on power law shapes are the works by Santos and Lewis[3−9]. For the idealized situation of two-dimensional rarefied hypersonic flow, they found that the stagnation point heating behavior for power law leading edges with finite radius of curvature ($n = 1/2$) followed that predicted for classical blunt body; the heating rate on blunt bodies is inversely proportional to the square root of curvature radius at the stagnation point. For those power law leading edges with zero radii of curvature ($n > 1/2$), it was found that the stagnation point heating is not a function of the curvature radius in the vicinity of the leading edges, but agreed with the classical blunt body behavior predicted by the continuum flow far from the stagnation point. Results were compared to a corresponding circular cylinder to determine which geometry would be better suited as a blunting profile. Their analysis also showed that power law shapes provided smaller total

drag and smaller shock wave standoff distance than the circular cylinder, typically used in blunting sharp leading edges for heat transfer considerations. However, circular cylinder provided smaller stagnation point heating than the power law shapes under the range of conditions investigated.

In order to improve the stagnation point heating of power law shapes, a modification was introduced into the power law leading edge. The new leading edge is composed by a flat nose followed by an afterbody surface defined by a power law shape, the flat-nose power-law leading edge. This concept is based on the work of Reller[17], who showed that a method of designing low heat transfer bodies is devised on the premise that the rate of heat transfer to the nose will be low if the local velocity is low, while the rate of heat transfer to the afterbody will be low if the local density is low. A typical body that results from this design method consists of a flat nose followed by a highly curved, but for the most part slightly inclined, afterbody surface.

In this context, Santos[18] has examined the aerodynamic surface quantities for a family of these new contours, flat-nose power-law leading edges. The emphasis of the work was to compare the performance of these new contours with that for power law leading edges with zero-thickness nose (Santos and Lewis[3]). The thickness effect was examined for a range of Knudsen number, Kn_t, based on the leading edge thickness, covering from the transitional flow regime to the free molecular flow one. It was examined a group of shapes that combined Kn_t of 1, 10 and 100 and power law exponents of 2/3, 0.7, 3/4 and 0.8. The analysis showed that flat-nose power-law leading edges provided much smaller stagnation point heating and slightly larger total drag than the power law shapes (zero-thickness nose) under the range of conditions investigated.

In an effort to obtain further insight into the nature of the aerothermodynamic characteristics of the flat-nose power-law shapes under hypersonic transitional flow conditions, this work extends the analysis presented by Santos[18] by comparing these flat-nose shapes with round leading edges in order to provide information on how well these shapes stand up as possible candidates for blunting geometries of hypersonic leading edges. Comparison based on geometry, stagnation point heating, total drag and shock standoff distance are made to examine the benefits and disadvantages of using flat-nose power-law shapes over round leading edges, used in blunting sharp leading edges for heat transfer considerations. Two method of comparison will be investigated: (1) flat-nose power-law shapes are compared to a corresponding round leading edge, which generates the power law shapes, and (2) flat-nose power-law shapes are compared to an equivalent round leading edge, which is generated from the computational results for the flat-nose power-law shapes. The equivalent round leading edge will yield the same stagnation point heating, the same drag coefficient or the same shock wave standoff distance as the computed solutions presented for flat-nose power-law shapes. Thus, for the equivalent stagnation point heating, for instance, the total drag coefficient and the shock standoff distance will be the basis of comparison between these leading edges, and these properties will determine which geometry performs better.

The present study is focused on the low-density region in the upper atmosphere, where the non-equilibrium conditions are such that traditional CFD calculations are inappropriate to yield accurate results. In such a circumstance, the DSMC method[19] will be employed to calculate the rarefied hypersonic two-dimensional flow on the leading edge shapes.

II. Leading Edge Geometry Definition

In dimensional form, the power law contours that define the shapes of the afterbody surfaces are given by the following expression,

$$y = y_{nose} + ax^n \tag{1}$$

where y_{nose} is the half thickness of the flat nose of the leading edges, n is the power law exponent and a is the power law constant which is a function of n.

The flat-nose power-law shapes are modeled by assuming a sharp leading edge (wedge) of half angle θ with a circular cylinder of radius R inscribed tangent to this wedge. The flat-nose power-law shapes, inscribed between the wedge and the cylinder, are also tangent to both shapes at the same common point where they

have the same slope angle. It was assumed a leading edge half angle of 10 degree, a circular cylinder diameter of 10^{-2}m, power law exponents of 2/3, 0.7, 3/4, and 0.8, and frontal surface thickness t/λ_∞ of 0, 0.01, 0.1 and 1, where $t = 2y_{nose}$ and λ_∞ is the freestream molecular mean free path. Figure 1 shows schematically this construction.

From geometric considerations, the power law constant a is obtained by matching slope on the wedge, circular cylinder and flat-nose power-law body at the tangency point. The common body height H at the tangency point is equal to $2R\cos\theta$, and the body length L from the nose to the tangency point in the axis of symmetry is given by $n(H-t)/2\tan\theta$. It was assumed that the leading edges are infinitely long but only the length L is considered, since the wake region behind the bodies is not of interest in this investigation.

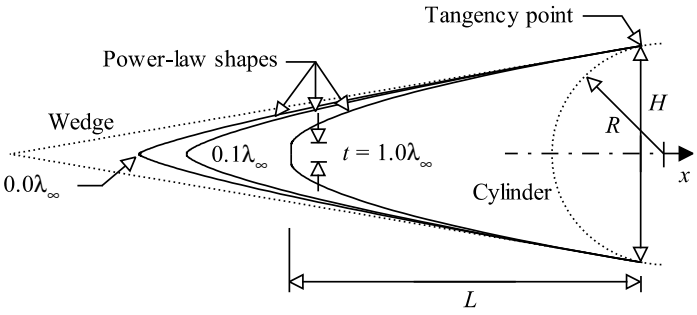

Figure 1. Drawing illustrating the leading edge geometries.

III. Methodology

Rarefaction effects and various non-equilibrium effects must be taken into account for the accurate analysis of the flow around vehicles operating at high altitudes. As a result, continuum gasdynamics, which is based on the concept of local equilibrium, may not be appropriate, and an approach based on molecular gasdynamics is required. Of the various methods for the analysis of low-density/high altitude flows, the Direct Simulation Monte Carlo (DSMC) method introduced by Bird[19] is the most accurate and credible procedure for computing complex problems.

In the DSMC method, the gasdynamics are modeled directly by the motion of a large number of statistically representative particles, each one with a position, velocity and internal energy. The state of the particles is stored and modified with time as the particles move, collide, and undergo boundary interactions in simulated physical space.

The molecular collisions are simulated with the variable hard sphere (VHS) molecular model[20] and the no time counter (NTC) collision sampling technique[21]. The energy exchange between kinetic and internal modes is controlled by the Borgnakke-Larsen statistical model[22]. Simulations are performed using a non-reacting gas model consisting of two chemical species, N_2 and O_2. Energy exchanges between the translational, rotational and vibrational modes are considered. The rate of rotational and vibrational relaxation are dictated by collision numbers Z_R and Z_V, respectively. Constant collision numbers of 5 and 50 are given for rotation and vibration, respectively.

In order to implement the particle-particle collisions, the flowfield is divided into an arbitrary number of regions, which are subdivided into computational cells that provide a convenient reference sampling of the macroscopic gas properties. The cells are further subdivided into four subcells, two subcells/cell in each direction, for the establishment of the collision rate. The dimensions of the cells must be such that the change in flow properties across each cell is small. The linear dimensions of the cells should be small in comparison with the scale length of the macroscopic flow gradients normal to streamwise directions, which means that the cell dimensions should be of the order of the local mean free path or even smaller[23−24].

The computational domain used for the calculation is made large enough upstream of the body to provide ample opportunity for freestream molecules to interact with those molecules that have reflected from the leading edge surface and are diffusing into the flow. A schematic view of the computational domain is depicted in Fig. 2. The DSMC method requires boundary conditions to be specified at all inflow and outflow boundaries. Side I is defined by the body surface. Diffuse reflection with complete thermal accommodation

is the condition applied to this side. Advantage of the flow symmetry is taken into account, and molecular simulation is applied to one-half of a full configuration. Thus, side II is a plane of symmetry. In such a boundary, all flow gradients normal to the plane are zero. At the molecular level, this plane is equivalent to a specular reflecting boundary. Side III is the freestream side through which simulated molecules enter and exit. Finally, side IV is the downstream outflow boundary. For hypersonic flow, a vacuum boundary condition is suitable since the flow velocities are generally high enough to prevent a significant number of particles from entering the flowfield at such boundary[25].

Numerical accuracy in DSMC method depends on the time step, on the cell size, and on the number of particles per computational cell. The method has been shown to be very accurate if the time step is small enough, compared to the mean collision time[26−27], the cell size is on the order of a local mean free path and there are sufficient computational particles per cell in order to minimize a statistical bias. These effects were investigated to determine the number of cells and the number of particles required to achieve grid independence solutions. Grid independence was tested by running the calculations with half and double the number of cells in each direction compared to a standard grid. Solutions were near identical for all grids used and were considered fully grid independent. A discussion of these effects on the aerodynamic surface quantities for power law shapes with zero-thickness nose ($t/\lambda_\infty = 0$) is described in details in Santos and Lewis[7]. The same procedure was adopted for the $t/\lambda_\infty > 0$ cases. However, the discussion will not be presented here.

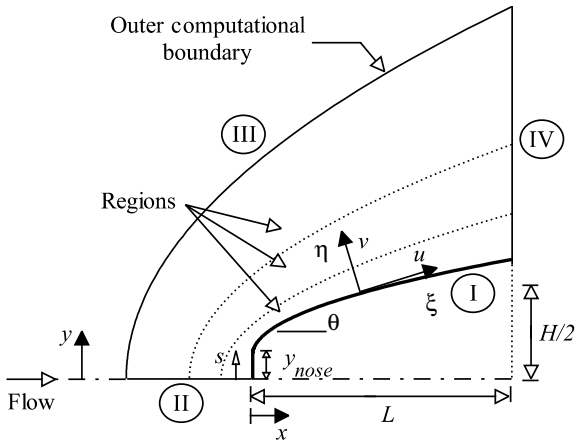

Figure 2. Schematic view of the computational domain.

IV. Flow Conditions

The freestream flow conditions used for the numerical simulation of flow past the leading edges are those given by Santos[18] and summarized in Table 1, and the gas properties[19] are shown in Table 2.

The freestream velocity V_∞ is assumed to be constant at 3.5 km/s, which corresponds to a freestream Mach number M_∞ of 12. The leading edge surface has a constant wall temperature T_w of 880 K for all cases considered. The freestream Reynolds number by unit meter Re_∞ is 21455 based on conditions in the undisturbed stream.

Table 1. Freestream flow conditions

Altitude (km)	T_∞(K)	p_∞(N/m^2)	ρ_∞(kg/m^3)	μ_∞(Ns/m^2)	n_∞(m^{-3})	λ_∞(m)
70	220.0	5.582	8.753×10^{-5}	1.455×10^{-5}	1.8209×10^{21}	9.03×10^{-4}

The overall Knudsen number Kn is defined as the ratio of the molecular mean free path λ in the freestream gas to a characteristic dimension of the flowfield. Hence, the characteristic dimension was defined as being the frontal surface thickness t of the leading edges. For the thicknesses investigated, $t/\lambda_\infty = 0$, 0.01, 0.1 and 1, the overall Knudsen numbers correspond to $Kn_t = \infty$, 100, 10 and 1, respectively. It should be noticed that $Kn_t = \infty$ case corresponds to the power law leading edge set already investigated by Santos and Lewis[3].

Table 2. Gas properties

	X mole fraction	m molecular mass, kg	d molecular diameter, m	ω viscosity index
O_2	0.237	5.312×10^{-26}	4.01×10^{-10}	0.77
N_2	0.763	4.650×10^{-26}	4.11×10^{-10}	0.74

V. Computational Results and Discussion

The purpose of this section is to discuss differences in the heat transfer, total drag and shock standoff distance due to variations on the leading edge thickness and on the afterbody shape, and to compare them to round shapes. Comparisons based on geometry are made to examine the benefits and disadvantages of using these blunt geometries over round shapes.

In order to present the comparison coherently, it is necessary to repeat the results of previous publication to some extent. In doing so this section begins with part of the results for power law shapes presented by Santos[18].

A. Flat-Nose Shape

The heat flux q_w to the body surface is calculated by the net energy flux of the molecules impinging on the surface. The net heat flux is related to the sum of the translational, rotational and vibrational energies of both incident and reflected molecules. A flux is regarded as positive if it is directed toward the surface. The heat flux is normalized by the freestream kinetic energy flux $\rho_\infty V_\infty^3/2$ and presented in terms of heat transfer coefficient C_h.

The heat flux q_w to the body surface was defined in terms of the incident and reflected flow properties, and based upon the gas-surface interaction model of fully accommodated, complete diffuse re-emission. The diffuse model assumes that the molecules are reflected equally in all directions, quite independently of their incident speed and direction. Due to the diffuse reflection model, the reflected velocity of the molecules impinging on the surface is obtained from a Maxwellian distribution that takes into account for the temperature of the body surface. In this fashion, as the wall temperature is the same for all the cases investigated, the number of molecules impinging on the surface plays the important role on the reflected contribution to the net heat flux to the body surface.

The leading edge nose thickness effect on heat transfer coefficient C_h is plotted from Figs. 3a to 3d for power law exponents of 2/3, 0.7, 3/4 and 0.8, respectively, as a function of the dimensionless distance $S(\equiv s/\lambda_\infty)$ along the surface measured from the stagnation point. For comparison purpose, the heat transfer coefficient C_h for the circular cylinder case is also shown as well as that one predicted by free molecular flow. It is seen from these figures that the heat transfer coefficient C_h is sensitive to the nose thickness as well as to the afterbody shape. As would be expected, the flatter the leading edge is the lower the heat transfer coefficient at the stagnation point. Also, the heat transfer coefficient remains essentially constant over the first half of the frontal surface, but then increases in the vicinity of the flat-face/afterbody junction for the flattest case investigated, $Kn_t = 1$ $(t/\lambda_\infty = 1)$. Subsequently, the heat transfer coefficient decreases sharply and continues to decline along the body surface.

Usually, the stagnation region is generally considered as being one of the most thermally stressed zones in sharp/blunt bodies, as shown by the power law cases, defined by $Kn_t = \infty$ $(t/\lambda_\infty = 0)$, investigated by Santos and Lewis[3]. Nevertheless, as a flat nose is introduced in these power law shapes, the most severe heat transfer region moves to the flat-face/afterbody junction with the nose thickness rise. The net heat flux

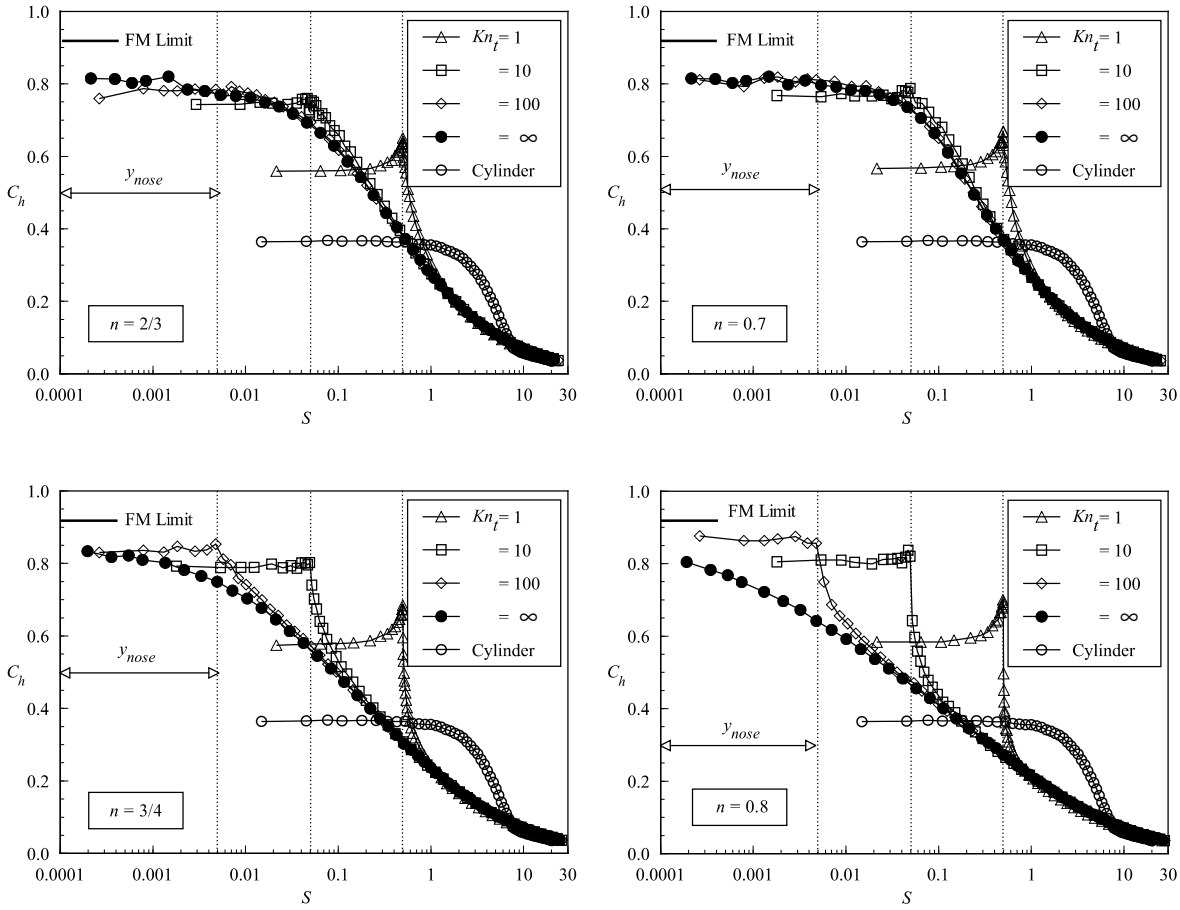

Figure 3. Heat transfer coefficient along the body surface as a function of the Knudsen number Kn_t for exponent n of (a) 2/3, (b) 0.7, (c) 3/4 and (d) 0.8.

depends on the number of molecules impinging on the body surface and on the velocity of the molecules. As shown by Santos[18], the number of molecules impinging on the front surface decreases in the vicinity of the flat-face/afterbody junction, then the velocity of the molecules increases as the flow approaches the junction of the leading edge in order to increase the heat transfer coefficient. Moreover, the contribution of the translational energy to the net heat flux varies with the square of the velocity of the molecules.

The heat transfer coefficient at the stagnation point predicted by the free molecular equations[19] is C_{ho} = 0.912, as shown in Fig. 3. According to this figure, the stagnation point heating tends to this limit value as the leading edge becomes sharp, i.e., by reducing the nose thickness of the leading edges (increasing Kn_t) and by increasing the power law exponent n.

In contrast to the power law bodies, the heat transfer coefficient C_h for the circular cylinder remains essentially constant over the first half of the cylindrically portion of the leading edge, but then decreases sharply up to the cylinder/wedge junction. In addition, the heat transfer coefficient over the circular cylinder varies by an order of magnitude from the stagnation point to the cylinder/wedge junction.

At this point, it seems important to compare the heat transfer coefficient at the stagnation point for the

flat-nose power-law shapes $(C_{ho})_{pwr}$ with that for the circular cylinder $(C_{ho})_{cyl}$ that generated the power law shapes. Table 3 displays the ratio of $(C_{ho})_{pwr}$ to $(C_{ho})_{cyl} = 0.366$ for the cases investigated as a function of the Knudsen number Kn_t. According to Table 3, a substantial reduction in the heat transfer coefficient at the stagnation point is obtained by introducing the flat nose in the power law shapes. As a reference, for power law exponent of 2/3, $(C_{ho})_{pwr}$ reduces from around 2.1 times to 1.5 times, compared to $(C_{ho})_{cyl}$, when the dimensionless nose thickness t/λ_∞ increases from 0 to 1. It is also noted that a similar behavior is obtained to power law exponent of 0.8, changing from 2.4 times to around 1.6 times for the same variation in the nose thickness.

Referring to Table 3, it is also observed a considerable reduction in the heat transfer coefficients of the new power law shapes when they are compared to the corresponding zero-thickness cases. For the zero-thickness cases, the heat transfer coefficient increased by around 12% as the power law exponent increased from 2/3 to 0.8. In contrast, for the $t/\lambda_\infty = 1$ case, the heat transfer coefficient increased only 4.5% as the power law exponent increased from 2/3 to 0.8.

Table 3. Heat transfer coefficient comparison at the stagnation point, $(C_{ho})_{pwr}/(C_{ho})_{cyl}$.

n	$Kn_t = \infty$	$Kn_t = 100$	$Kn_t = 10$	$Kn_t = 1$
2/3	2.145	2.123	2.033	1.527
0.7	2.243	2.235	2.098	1.549
3/4	2.344	2.273	2.156	1.574
0.8	2.402	2.374	2.205	1.596

The drag on a surface in a gas flow results from the interchange of momentum between the surface and the molecules colliding with the surface. The total drag is obtained by the integration of the pressure p_w and shear stress τ_w distributions along the body surface. In an effort to understand the effects of the pressure and the shear stress acting on the surface of the flat-nose leading edges, both forces will be presented before the total drag.

The pressure p_w on the body surface is calculated by the sum of the normal momentum fluxes of both incident and reflected molecules at each time step. Results are normalized and presented in terms of pressure coefficient C_p.

The variation of the pressure coefficient C_p caused by changes in the leading edge nose thickness is demonstrated in Figs. 4a and 4b for power law exponents of 2/3 and 3/4, respectively. The pressure coefficient for power law exponents of 0.6 and 0.8 omitted here is discussed in details in Santos[18]. It can be noted from these figures that the pressure coefficient is high along the frontal surface, basically a constant value along it, and decreases dramatically along the afterbory surface in the vicinity of the flat-face/afterbody junction. This effect is more pronounced with decreasing Knudsen number Kn_t, i.e., as the nose becomes flatter.

Plotted along with the computational solution for pressure coefficient is the pressure coefficient predicted by the free molecular flow equations and that for the circular cylinder. For the circular cylinder case, the pressure coefficient C_p follows the same trend presented by the heat transfer coefficient in that it remains constant over the first half of the cylindrically portion of the leading edge, but then decreases sharply up to the cylinder/wedge junction. Also, the pressure coefficient C_p varies by one order of magnitude from the stagnation point to the cylinder/wedge junction.

The pressure coefficient C_p predicted by the free molecular flow equations on the front surface is 2.35. For the thinnest flat-nose leading edge investigated, $t/\lambda_\infty = 0.01$, which corresponds to $Kn_t = 100$, and for power law exponent of 0.8, the flow seems to approach the free collision flow in the vicinity of the stagnation point (Santos[18]), as was pointed out earlier.

The shear stress τ_w on the body surface is calculated by averaging the tangential momentum transfer of the molecules impinging on the surface. For the diffuse reflection model imposed for the gas-surface interaction, reflected molecules have a tangential moment equal to zero, since the molecules essentially lose, on average, their tangential velocity component. The shear stress τ_w is normalized by the freestream dynamic pressure $\rho_\infty V_\infty^2/2$ and presented in terms of the skin-friction coefficient C_f.

The influence of the leading edge nose thickness on the skin friction coefficient obtained by DSMC method is displayed in Figs. 5a and 5b for power law exponents of 2/3 and 3/4, respectively, and parameterized by

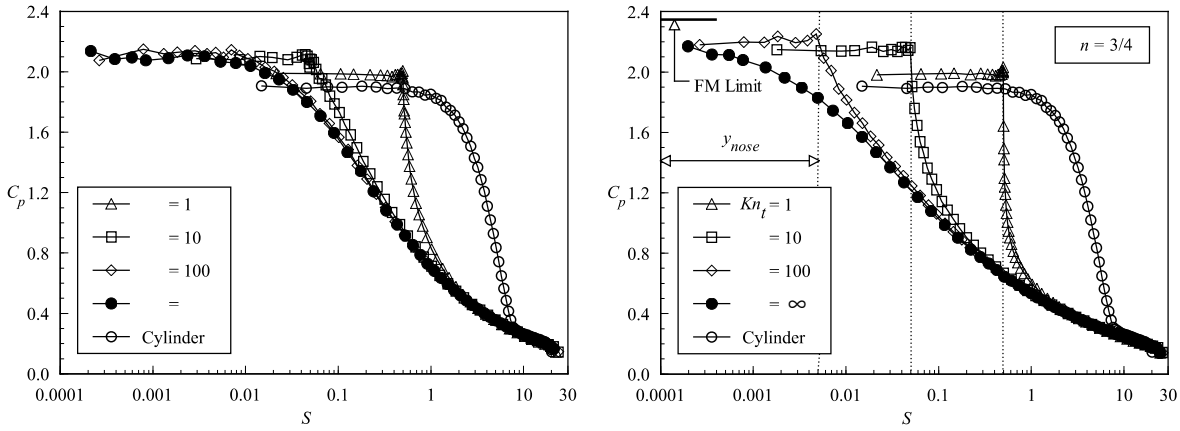

Figure 4. Pressure coefficient along the body surface as a function of the Knudsen number Kn_t for exponent n of (a) 2/3 and (b) 3/4.

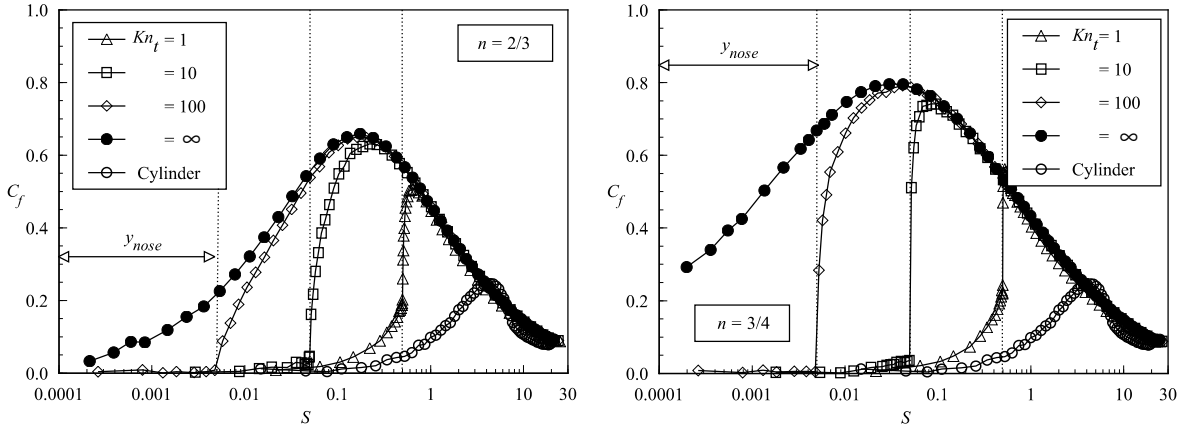

Figure 5. Skin friction coefficient along the body surface as a function of the Knudsen number Kn_t for exponent n of (a) 2/3 and (b) 3/4.

the thickness Knudsen number. According to these figures, the skin friction coefficient C_f is zero at the stagnation point and slightly increases along the frontal surface up to the flat-face/afterbody junction of the leading edge. After that, C_f increases meaningfully to a maximum value that depends on the nose thickness, and decreases downstream along the body surface by approaching the skin friction coefficient predicted by the reference case of zero thickness, $Kn_t = \infty$. In addition, smaller thickness t (larger Kn_t) leads to higher peak value for the skin friction coefficient C_f. Also, smaller thickness t displaces the peak value to near the flat-face/afterbody junction.

The skin friction coefficient C_f predicted by the free molecular flow equations[19] is zero along the frontal surface of the bodies and exhibits its maximum value on the afterbody surface at a station that corresponds to a body slope of 45 degree (not shown). Similarly, the maximum values of C_f for the nose thicknesses investigated occur very close to the same station. As the power law exponent n increases the arc length

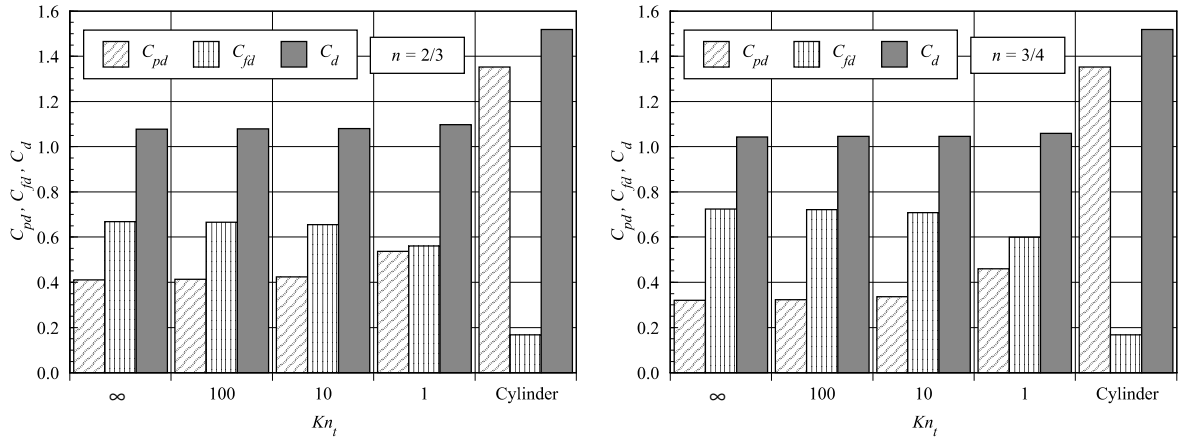

Figure 6. Pressure drag, skin friction drag and total drag coefficients along the body surface as a function of the Knudsen number Kn_t for exponent n of (a) 2/3 and (b) 3/4.

s/λ_∞ corresponding to a slope of 45 degree approaches the shoulder of the shapes.

The total drag is obtained by the integration of the pressure p_w and shear stress τ_w distributions from the nose of the leading edge to the station L (see Fig. 1), which corresponds to the tangent point common to all of the body shapes. The total drag presented in this section were obtained by assuming the shapes acting as leading edges. Consequently, no base pressure effects were taken into account on the calculations. The DSMC results for total drag are normalized by $\rho_\infty V_\infty^2 H/2$ and presented as total drag coefficient C_d and its components of pressure drag C_{pd} and skin friction drag C_{fd} coefficients.

The impact of the leading edge nose thickness on the total drag coefficient C_d is demonstrated in Figs. 6a and 6b for power law exponents of 2/3 and 3/4, respectively, along with the drag coefficient for the circular cylinder case. It is seen that as the leading edge becomes flatter the contribution of the pressure drag C_{pd} to the total drag increases and the contribution of the skin friction drag C_{fd} decreases. As the net effect on total drag coefficient C_d depends on these to opposite behaviors, hence no appreciable changes are observed in the total drag coefficient for the nose thicknesses investigated. The total drag for the two other cases, $n =$ 0.6 and 0.8, follows the same trend observed for those shown in Fig. 6.

Referring to Fig. 6, it can be seen that the total drag coefficient C_d increased slightly by a rise in the nose thickness t. The major contribution to the total drag coefficient is attributed to the skin friction coefficient, which decreases with increasing the nose thickness t. In contrast, for the circular cylinder case, the major contribution to the total drag coefficient is attributed to the pressure, that accounts for 89% of the total drag.

At this point, it seems important to compare the total drag coefficient of the flat-nose power-law shapes $(C_d)_{pwr}$ with that for the circular cylinder $(C_d)_{cyl}$ that generated the power law shapes. Table 4 illustrates the ratio of $(C_d)_{pwr}$ to $(C_d)_{cyl} = 1.519$ for the cases investigated as a function of the Knudsen number Kn_t. According to Table 4, no substantial changes are observed in the total drag coefficient by introducing the flat nose in the power law shapes. As a reference, for power law exponent of 2/3, $(C_d)_{pwr}$ increases from 71.0% to only 72.3%, compared to $(C_d)_{cyl}$, when the dimensionless nose thickness t/λ_∞ increases from 0 to 1. It is also noted that a similar behavior is obtained to power law exponent of 0.8, changing from 67.6% to 68.5% for the same variation in the nose thickness. It means that the total drag only increases 1.8% and 1.3% to cases $n = 2/3$ and 0.8, respectively. On the other hand, a significantly reduction is observed in the stagnation point heating for the same cases.

The shock wave standoff distances for flat-nose power-law shapes have been already calculated by

Santos[28], where the procedure used in order to obtain them is described in details. Therefore, only the results will be presented in this work.

Table 5 displays the shock wave standoff distance Δ, normalized by λ_∞, for the flat-nose power-law leading edges investigated. According to this table, there is a discrete shock standoff distance for all cases investigated. Moreover, the shock standoff distance decreases with increasing the power law exponent n; as the leading edge becomes aerodynamically sharp. Compared to power law shapes, the reference circular cylinder provides a larger shock detachment, Δ/λ_∞ of 1.645. This value is about 5 times larger than that for the $n = 2/3$ case and is one order of magnitude larger then that for the $n = 0.8$ case by considering zero-thickness nose. These values reduce to around 2.3 and 2.5 times for the same cases with thickness t/λ_∞ of 1.

Table 4. Comparison of the total drag coefficient for flat-nose power-law shapes with that for the circular cylinder, $(C_d)_{pwr}/(C_d)_{cyl}$.

n	$Kn_t = \infty$	$Kn_t = 100$	$Kn_t = 10$	$Kn_t = 1$
2/3	0.710	0.711	0.711	0.723
0.7	0.716	0.716	0.716	0.724
3/4	0.687	0.688	0.688	0.697
0.8	0.676	0.677	0.677	0.685

The displacement of the shock wave is especially undesirable in a waverider geometry, because this hypersonic configuration usually depends on shock wave attachment at the leading edge to achieve its high lift-to-drag ratio at high-lift coefficient. Shock wave detachment will allow pressure leakage from the lower surface of the vehicle to the upper surface, thereby degrading the aerodynamic performance of the vehicle. In this context, the power law leading edges seem to be more appropriate than the reference circular cylinder, since they present reduced shock wave detachment distances as compared to the circular cylinder.

Table 5. Dimensionless shock wave standoff distance Δ/λ_∞ for flat-nose power-law leading edges.

n	$Kn_t = \infty$	$Kn_t = 100$	$Kn_t = 10$	$Kn_t = 1$
2/3	0.330	0.352	0.401	0.708
0.7	0.289	0.312	0.358	0.676
3/4	0.216	0.237	0.312	0.654
0.8	0.166	0.187	0.271	0.640

B. Round Leading Edge

In order to compare flat-nose power-law leading edge with round leading edge, it becomes necessary to determine the dependence of heat transfer, total drag and shock standoff distance for round leading edge on the nose radius. In this connection, DSMC simulations were performed for four round leading edges, besides the reference round leading edge (circular cylinder), with nose radii R_N/λ_∞ of 0.02, 0.1, 1.0, and 2.0, which correspond to overall Knudsen number Kn_D of 25, 5, 0.5 and 0.25, respectively, by assuming the nose diameter as the characteristic length.

Distributions of the heat transfer coefficient C_h along the round leading edge surface are illustrated in Fig. 7a with the dimensionless nose radius R_N/λ_∞ as a parameter. It is observed from this figure that altering the nose radius produces a substantial change in the heat transfer coefficient in the cylindrically blunt portion of the leading edge, provided that the gas-surface interaction is diffuse. The heat transfer coefficient presents the maximum value in the stagnation point and drops off sharply along the cylindrically blunt portion up to the cylinder/wedge junction. Also, the heat transfer coefficient in the stagnation region decreases with increasing the nose radius. This behavior seems to be in agreement with the continuum predictions for blunt body in that the heat flux scales inversely with the square root of the nose radius.

The nose radius effect can also be seen in a different way by comparing the DSMC computational results with those calculated by assuming free molecular flow. Figure 7b presents this comparison for the heat transfer coefficient as a function of the body slope angle θ. Similarly to power law shapes, these curves indicate that the heat transfer coefficient also approaches the free molecular limit ($C_{ho} = 0.915$) in the

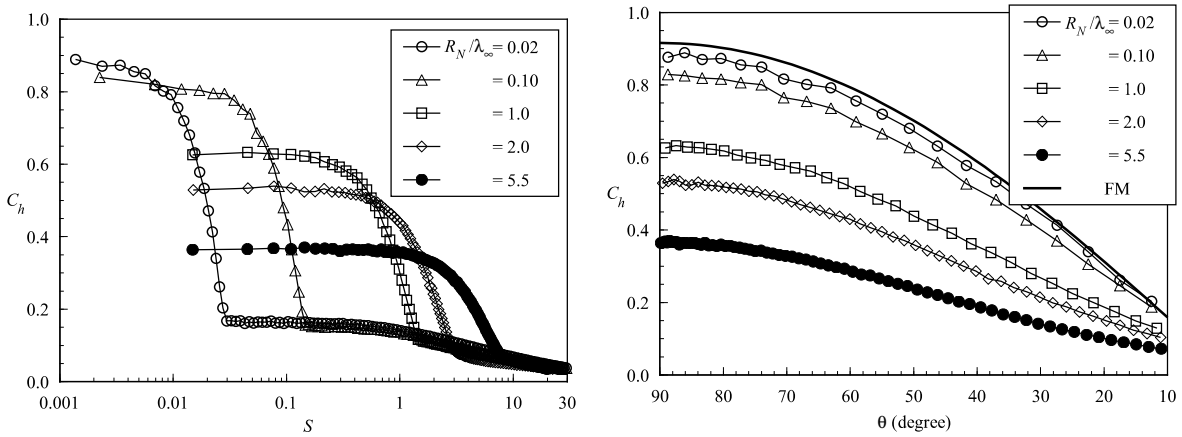

Figure 7. Heat transfer coefficient C_h along (a) the round leading edge surface as a function of the arc length S and (b) the cylindrically blunt portion of the round leading edge as a function of the body slope angle θ.

cylindrically portion of the round leading edge with reducing the nose radius. As expected, by reducing the nose radius the leading edge becomes sharper and approaches the wedge leading edge shown in Fig. 1.

The heat transfer coefficient at the stagnation point C_{ho} is displayed in Table 6 for the nose radii investigated. These values were obtained by a curve fitting process performed over the curves displayed in Fig. 7b.

Distributions of the pressure coefficient C_p along the body surface for different nose radii are depicted in Fig. 8a. According to this figure, it is seen that the pressure coefficient follows the same trend as that presented by the heat transfer coefficient. The pressure coefficient presents the maximum value at the stagnation point and decreases fast in the cylindrically blunt portion of the leading edge. It is also verified that the pressure coefficient in the cylindrically blunt portion is one order of magnitude higher than the pressure coefficient in the wedge portion of the leading edge.

The pressure coefficient C_p acting on the cylindrically blunt portion of the leading edges is compared to that predicted by free molecular flow in Fig. 8b, with the nose radius as a parameter. It is noted from this figure that the pressure coefficient also approaches that one predicted by free molecular flow (C_{po} = 2.35) for the smallest nose radius investigated, which corresponds to an overall Knudsen number Kn_D of 25.

Variations of the skin friction coefficient C_f caused by changes in the nose radius of the leading edge are demonstrated in Fig. 9a as a function of the dimensionless arc length S. As can be seen, the skin friction coefficient increases from zero at the stagnation point to a maximum value that is located in the cylindrically blunt portion of the leading edge, and decreases downstream along the body surface.

The skin friction coefficient C_f from computational solution can be also compared to that predicted by considering free molecular flow. Figure 9b shows the comparison for the cylindrically portion of the leading

Table 6. Heat transfer coefficient at the stagnation point C_{ho} for round leading edges.

R_N/λ_∞	0.02	0.1	1.0	2.0	5.5
C_{ho}	0.883	0.824	0.630	0.532	0.366

Table 7. Dimensionless shock wave standoff distance Δ/λ_∞ for round leading edges.

R_N/λ_∞	0.02	0.1	1.0	2.0	5.5
Δ/λ_∞	0.114	0.226	0.598	0.845	1.646

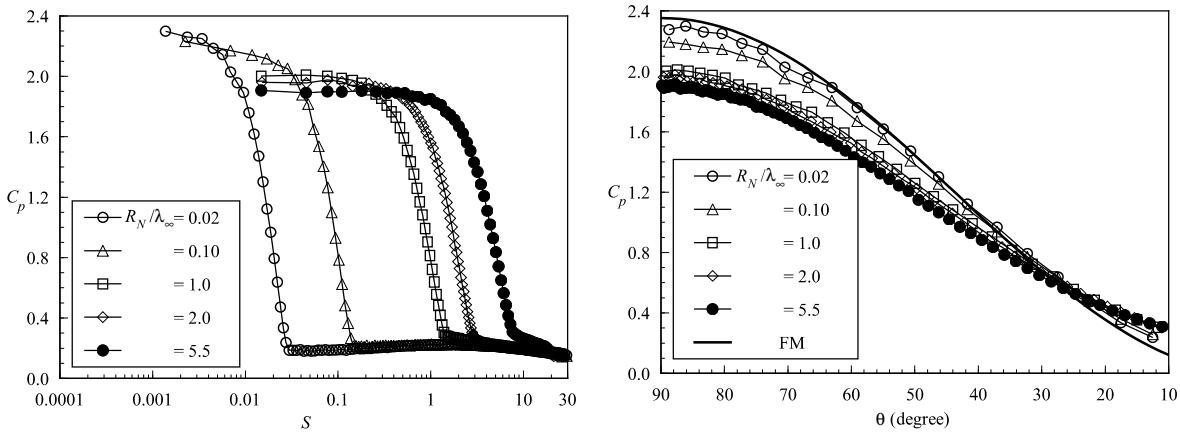

Figure 8. Pressure coefficient C_p along (a) the round leading edge surface as a function of the arc length S and (b) the cylindrically blunt portion of the round leading edge as a function of the body slope angle θ.

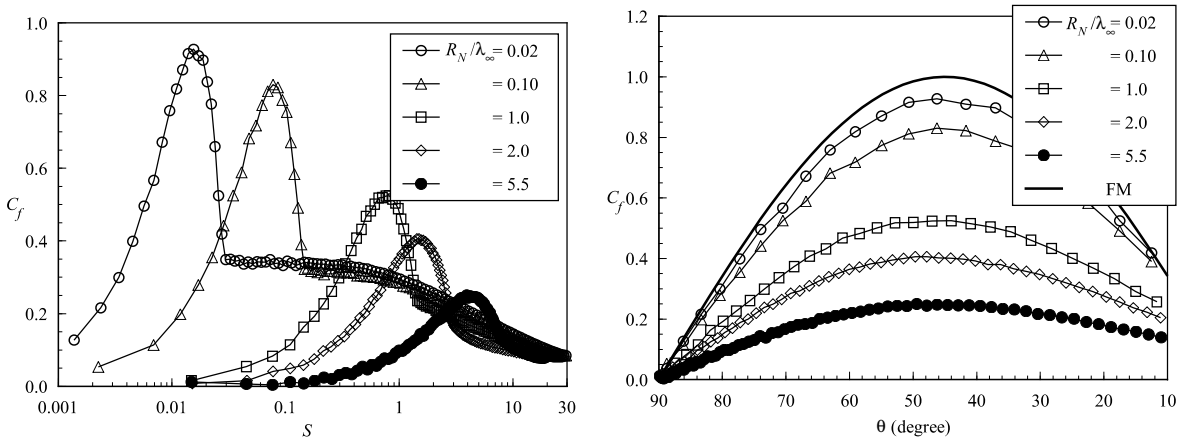

Figure 9. Skin friction coefficient C_f along (a) the round leading edge surface as a function of the arc length S and (b) the cylindrically blunt portion of the round leading edge as a function of the body slope angle θ.

edges as a function of the body slope angle θ. It is recognized that the round leading edges also exhibit the maximum value for the skin friction coefficient around a 45-degree station.

The dependence of the total drag coefficient C_d on the nose radius is depicted in Fig. 10. In this figure, the contributions of the pressure drag C_{pd} and the skin friction drag C_{fd} coefficients are also shown. As would be expected, the total drag for round leading edges approaches the wedge drag with decreasing the nose radius.

The dimensionless shock wave standoff distance Δ/λ_∞ for round leading edges is shown in Table 7. Similarly to flat-nose power-law leading edges, there is a discrete shock standoff distance for the round leading edge cases investigated. In addition, the shock standoff distance decreases with diminishing the nose radius. This is an expected result since shock standoff distance on a cylinder scales with the curvature radius.

C. Equivalent Nose Radius

The stagnation point heating, the total drag and the shock wave standoff distance for flat-nose power-law leading edges have been compared to those for the reference round leading edge (circular cylinder) in the previous sections.

A second means of comparison between flat-nose power-law shapes and round leading edges is defined as equivalent round leading edge. Equivalent round leading edges, or equivalent nose radii, are found that have the same value for the stagnation point heating, total drag or shock standoff distance provided by the flat-nose power-law leading edges. For instance, by holding the stagnation point heating the same, the total drag and the shock standoff distance on the equivalent round leading edge may be compared to those for flat-nose power-law leading edges in order to determine which shape is better suited for leading-edge blunting. A similar procedure is repeated for the total drag and for the shock standoff distance.

A summary of the computed data for the heat transfer coefficient at the stagnation point C_{ho}, the total drag coefficient C_d and the shock standoff distance Δ/λ_∞ for round leading edge is displayed in Fig. 11.

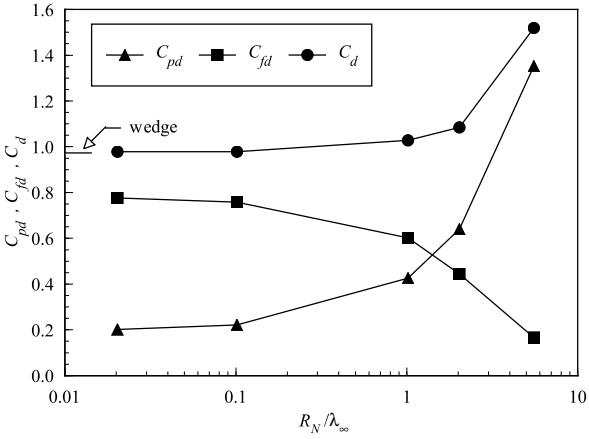

Figure 10. Total drag coefficient for round leading edges as a function of the nose radius.

The stagnation point heating C_{ho} for each one of the flat-nose power-law shapes displayed in Table 3 is used as an input in Fig. 11 in order to determine the equivalent nose radius $R_{N,eqv}$. With the equivalent nose radius, the total drag and the shock standoff distance that correspond to that equivalent nose radius are also obtained from Fig. 11 itself.

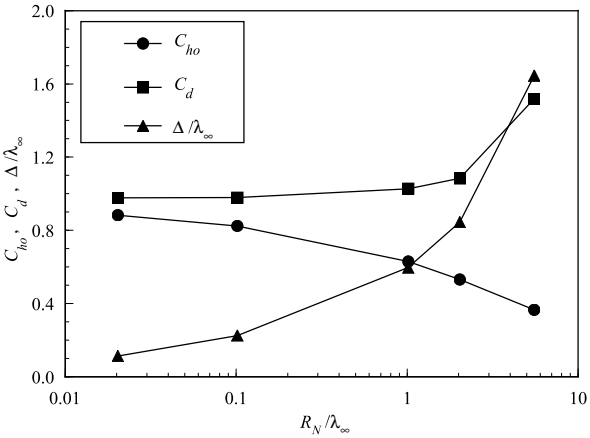

Figure 11. Heat transfer coefficient at the stagnation point C_{ho}, total drag C_d and the shock standoff distance Δ/λ_∞ for round leading edges as a function of the nose radius.

The comparison of the total drag coefficient and the shock standoff distance for flat-nose power-law shapes and for round leading edges with equivalent nose radii that match flat-nose power-law body stagnation point heating is shown in Table 8. It is seen from Table 8 that equivalent round leading edges have slightly lower drag and smaller shock standoff distance than flat-nose power-law bodies for the majority of the cases investigated. Nevertheless, in general, flat-nose power-law bodies perform better for the $Kn_t = 1$ case, which corresponds to nose thickness $t/\lambda_\infty = 1$. As a reference, the case $n = 2/3$ and $Kn_t = 1$, which is tangent to a 10-degree wedge (see Fig. 1), has the same stagnation point heating as a round leading edge that is 3.17 times smaller than the reference round leading edge that is also tangent to the wedge at the same point. Furthermore, this equivalent round leading edge has a shock standoff distance that is 9.6% larger than the corresponding flat-nose power-law body. As a result, based on Table 8, for the same stagnation point heating, round leading edges perform better than flat-nose power-law

bodies for those cases with nose thickness smaller than the freestream mean free path.

By using the total drag coefficient C_d found previously for flat-nose power-law leading edges, Table 4, an equivalent nose radius $R_{N,eqv}$ may be found from Fig. 11 that gives the same total drag coefficient as the flat-nose power-law bodies. At this time, the stagnation point heating and the shock standoff distance will be the two important factors in order to determine which shape is better suited for leading-edge blunting.

The comparison of the stagnation point heating and the shock standoff distance for flat-nose power-law shapes and for round leading edges with equivalent nose radii that match flat-nose power-law body total drag is tabulated in Table 9. It is clear from Table 9 that equivalent round leading edges have lower stagnation point heating than the flat-nose power-law bodies. Nonetheless, the equivalent round leading edges have much larger shock standoff distances than flat-nose power-law shapes. Again, by taking the case $n = 2/3$ and $Kn_t = 1$ as a reference, this shape has the same total drag as a round leading edge that is around 2.6 times smaller than the reference round leading edge. Also, this equivalent round leading edge has a stagnation point heating that is around 6% smaller than the corresponding flat-nose power-law body. In contrast, the equivalent round leading edge has a shock standoff distance that is 23% larger than that for the case $n = 2/3$ and $Kn_t = 1$. As a matter of fact, larger displacement of the shock wave is an undesirable property for hypersonic waverider design, as mentioned earlier. Consequently, based on Table 9, round leading edges perform worse than flat-nose power-law bodies as the shock standoff distance consideration is involved.

Table 8. Nose radius necessary for comparable stagnation point heating to flat-nose power-law shapes.

n	Kn_t	$\frac{R_{N,eqv}}{\lambda_\infty}$	$\frac{R}{R_{N,eqv}}$	$\frac{C_{d,eqv}}{C_{d,pwr}}$	$\frac{\Delta_{eqv}}{\Delta_{pwr}}$
2/3	∞	0.288	19.25	0.917	0.912
	100	0.323	17.13	0.918	0.897
	10	0.478	11.58	0.925	0.946
	1	1.747	3.17	0.973	1.096
0.7	∞	0.116	47.92	0.900	0.801
	100	0.131	42.33	0.902	0.762
	10	0.366	15.15	0.913	0.930
	1	1.665	3.33	0.968	1.119
3/4	∞	0.055	99.94	0.938	0.753
	100	0.091	60.96	0.936	0.890
	10	0.267	20.74	0.945	0.941
	1	1.571	3.52	0.999	1.121
0.8	∞	0.027	207.42	0.952	0.742
	100	0.040	139.05	0.951	0.754
	10	0.182	30.35	0.956	0.954
	1	1.488	3.72	1.013	1.115

Another interesting result may be found from the shock standoff distance. The equivalent nose radius $R_{N,eqv}$ that yields the same shock standoff distance Δ/λ_∞ for each one of the flat-nose power-law shapes, Table 5, may be determined from Fig. 11.

The comparison of the stagnation point heating and the total drag coefficient for flat-nose power-law shapes and for round leading edges with equivalent nose radii that match flat-nose power-law body shock standoff distance is tabulated in Table 10. It is apparent from Table 10 that equivalent round leading edges provide a better performance than flat-nose power-law shapes for nose thickness less than the freestream mean free path.

Finally, a critical assessment of the results provided by Tables 8, 9 and 10 confirms the expected behavior for sharp and blunt leading edges. As the leading edge shape approaches the wedge shape (see Fig. 1), the total drag decreases, the shock standoff distance decreases and the stagnation point heating increases. In contrast, as the leading edge shape approaches the circular cylinder, the total drag increases, the shock standoff distance increases and the stagnation point heating decreases. Thus, the ideal leading edge shape for hypersonic vehicle will depend on the context.

Table 9. Nose radius necessary for comparable total drag to flat-nose power-law shapes.

n	Kn_t	$\frac{R_{N,eqv}}{\lambda_\infty}$	$\frac{R}{R_{N,eqv}}$	$\frac{C_{ho,eqv}}{C_{ho,pwr}}$	$\frac{\Delta_{eqv}}{\Delta_{pwr}}$
2/3	∞	1.914	2.89	0.692	2.471
	100	1.932	2.87	0.696	2.330
	10	1.942	2.85	0.726	2.055
	1	2.138	2.59	0.942	1.228
0.7	∞	2.060	2.69	0.646	2.950
	100	2.050	2.70	0.649	2.726
	10	2.049	2.70	0.691	2.372
	1	2.148	2.58	0.928	1.290
3/4	∞	1.299	4.26	0.702	3.092
	100	1.325	4.18	0.721	2.838
	10	1.325	4.18	0.760	2.161
	1	1.581	3.50	0.998	1.125
0.8	∞	1.011	5.48	0.718	3.599
	100	1.030	5.38	0.723	3.215
	10	1.021	5.42	0.780	2.209
	1	1.243	4.46	1.041	1.021

VI. Concluding Remarks

Table 10. Nose radius necessary for comparable shock standoff distance to flat-nose power-law shapes.

n	Kn_t	$\frac{R_{N,eqv}}{\lambda_\infty}$	$\frac{R}{R_{N,eqv}}$	$\frac{C_{ho,eqv}}{C_{ho,pwr}}$	$\frac{C_{d,eqv}}{C_{d,pwr}}$
2/3	∞	0.359	15.43	0.981	0.921
	100	0.413	13.42	0.975	0.922
	10	0.532	10.41	0.985	0.928
	1	1.469	3.77	1.048	0.959
0.7	∞	0.256	21.59	0.963	0.906
	100	0.313	17.71	0.953	0.911
	10	0.427	12.98	0.983	0.916
	1	1.336	4.15	1.056	0.951
3/4	∞	0.094	58.79	0.967	0.938
	100	0.130	42.72	0.983	0.938
	10	0.312	17.72	0.988	0.947
	1	1.247	4.44	1.054	0.982
0.8	∞	0.058	95.84	0.974	0.952
	100	0.073	75.49	0.972	0.951
	10	0.213	25.98	0.992	0.958
	1	1.187	4.66	1.050	0.997

The computations of a rarefied hypersonic flow on blunt bodies have been performed by using the Direct Simulation Monte Carlo method. The calculations provided information concerning the nature of the stagnation point heating, the total drag and the shock standoff distance for a family of contours composed by a flat nose supplemented by a curved afterbody surface defined by power-law shapes.

The aerothermodynamic performance of these blunt shapes was compared to a corresponding circular cylinder, typically used in blunting sharp leading edges for heat transfer considerations. It was found that the total drag is lower and the shock standoff distance is much smaller on the new blunt shapes than on the representative circular cylinder solution in this geometric comparison. Nevertheless, stagnation point heating for these flat-nose shapes is still higher than that for the corresponding circular cylinder. These flat-nose shapes behave as if they had a sharper profile than their representative circular cylinder. However, these shapes have more volume than the circular cylinder geometry. Hence, although stagnation point heating on these new shapes may be higher as compared to the circular cylinder, the overall heat transfer to these leading edges may be tolerate if there is active cooling because additional coolant may be placed in the leading edge. Moreover, the shock standoff distance on a cylinder scales with the radius of curvature, therefore cylindrical bluntness added for heating rate reduction will also tend to displace the shock wave, allowing pressure leakage. In this context, as the new shapes behave as if they were sharper profiles than the circular cylinder, then they present a better performance since they display smaller shock detachment distances than the corresponding circular cylinder.

In addition, equivalent round leading edges were defined with the same stagnation point heating, total drag or shock standoff distance yielded by the flat-nose power-law shapes. With the same stagnation point heating as the flat-nose shapes, round leading edges were shown to produce slightly smaller total drag and smaller shock standoff distance for the majority of the cases investigated. The analysis also showed that, for the same total drag, round leading edges gave larger shock standoff distance than flat-nose shapes. For the equivalent shock standoff distance, the shapes exhibited approximately the same performance.

It is apparent that each comparison resulted in a different conclusion for which geometry perform better. Thus, the ideal blunting leading edge relies on the context. If shock standoff distance is the primary issue in leading edge design of hypersonic waveriders, then flat-nose power-law leading edges are superior to round leading edges.

VII. Acknowledgments

The financial support provided by Fundação de Amparo à Pesquisa do Estado de São Paulo (grant FAPESP 2003/01765-9) is gratefully acknowledged.

References

[1]O'Brien, T. F. and Lewis, M. J., "Power Law Shapes for Leading-Edge Blunting with Minimal Shock Standoff," *Journal of Spacecraft and Rockets*, Vol. 36, No. 5, 1999, pp. 653–658.

[2]Santos, W. F. N., "Direct Simulation Monte Carlo of Rarefied Hypersonic Flow on Power Law Shaped Leading Edges," Ph.D. Dissertation, Dept. of Aerospace Engineering, University of Maryland, College Park, MD, Dec., 2001.

[3]Santos, W. F. N., and Lewis, M. J., "Power Law Shaped Leading Edges in Rarefied Hypersonic Flow," *Journal of Spacecraft and Rockets*, Vol. 39, No. 6, 2002, pp. 917–925.

[4]Santos, W. F. N., and Lewis, M. J., "Angle of Attack Effect on Rarefied Hypersonic Flow over Power Law Shaped Leading Edges," in *23rd International Symposium on Rarefied Gas Dynamics*, Whistler, BC, Canada, July 20-25, 2002.

[5]Santos, W. F. N., and Lewis, M. J., "Shock Wave Structure in a Rarefied Hypersonic Flow on Power Law Shaped Leading Edges," in *41st AIAA Aerospace Sciences Meeting and Exhibit*, AIAA Paper 2003-1134, Reno, NV, January 6-9, 2003.

[6]Santos, W. F. N., and Lewis, M. J., "Aerodynamic Heating Performance of Power Law Leading Edges in Rarefied Hypersonic Flow," in *36th AIAA Thermophysics Conference*, AIAA Paper 2003-3894, Orlando, FL, June 23-26, 2003.

[7]Santos, W. F. N., and Lewis, M. J., "Effects of Compressibility on Rarefied Hypersonic Flow over Power Law Leading Edges," in *42nd AIAA Aerospace Sciences Meeting and Exhibit*, AIAA Paper 2004-1181, Reno, NV, January 5-8, 2004.

[8]Santos, W. F. N., and Lewis, M. J., "DSMC Calculations of Rarefied Hypersonic Flow over Power Law Leading Edges with Incomplete Surface Accommodation," in *34th AIAA Fluid Dynamics Conference and Exhibit*, AIAA Paper 2004–2636, Portland, OR, June 28–July 1, 2004.

[9]Santos, W. F. N., and Lewis, M. J., "Calculation of Shock Wave Structure over Power Law Bodies in Hypersonic Flow," *Journal of Spacecraft and Rockets*, To appear, in press.

[10]Boyd, I. D., and Padilla, J. F., "Simulation of Sharp Leading Edge Aerothermodynamic," in *12th AIAA International Space Planes and Hypersonic Systems and Technologies*, AIAA Paper 2003–7062, Norfolk, VA, December 15–19, 2003.

[11]Nonweiler, T. R. F., "Aerodynamic Problems of Manned Space Vehicles," *Journal of the Royal Aeronautical Society*, Vol. 63, Sept, 1959, pp. 521–528.

[12]Anderson, J. L., "Tethered Aerothermodynamic Research for Hypersonic Waveriders," in *Proceedings of the 1st International Hypersonic Waverider Symposium*, Univ. of Maryland, College Park, MD, 1990.

[13]Potter, J. L. and Rockaway, J. K., "Aerodynamic Optimization for Hypersonic Flight at Very High Altitudes," in *Rarefied gas Dynamics: Space Science and Engineering*, edited by B. D. Shizgal and D. P. Weaver, Vol. 160, Progress in Astronautics and Aeronautics, AIAA New York, 1994, pp.296-307.

[14]Rault, D. F. G., "Aerodynamic Characteristics of a Hypersonic Viscous Optimized Waverider at High Altitude," *Journal of Spacecraft and Rockets*, Vol. 31, No. 5, 1994, pp. 719–727.

[15]Graves, R. E. and Argrow, B. M., "Aerodynamic Performance of an Osculating-Cones Waverider at High Altitudes," in *35th AIAA Thermophysics Conference*, AIAA Paper 2001-2960, Anaheim, CA, 2001.

[16]Mason, W. H. and Lee, J., "Aerodynamically Blunt and Sharp Bodies," *Journal of Spacecraft and Rockets*, Vol. 31, No. 3, 1994, pp. 378–382.

[17]Reller Jr., J. O., "Heat Transfer to Blunt Nose Shapes with Laminar Boundary Layers at High Supersonic Speeds," NACA RM-A57FO3a, 1957.

[18]Santos, W. F. N., "Aerothermodynamic Characteristics of Flat-Nose Power-Law Bodies in Low-Density Hypersonic Flow," in *22nd AIAA Applied Aerodynamics Conference and Exhibit*, AIAA Paper 2004–5381, Providence, RI, August 16–19, 2004.

[19]Bird, G. A.,*Molecular Gas Dynamics and the Direct Simulation of Gas Flows*, Oxford University Press, Oxford, England, UK, 1994.

[20]Bird, G. A., "Monte Carlo Simulation in an Engineering Context," in *Progress in Astronautics and Aeronautics: Rarefied gas Dynamics*, edited by Sam S. Fisher, Vol. 74, part I, AIAA New York, 1981, pp. 239–255.

[21]Bird, G. A., "Perception of Numerical Method in Rarefied Gasdynamics, in *Rarefied gas Dynamics: Theoretical and Computational Techniques*," edited by E. P. Muntz, and D. P. Weaver and D. H. Capbell, Vol. 118, Progress in Astronautics and Aeronautics, AIAA, New York, 1989, pp. 374–395.

[22]Borgnakke, C. and Larsen, P. S., "Statistical Collision Model for Monte Carlo Simulation of Polyatomic Gas Mixture," *Journal of computational Physics*, Vol. 18, No. 4, 1975, pp. 405–420.

[23]Alexander, F. J., Garcia, A. L., and, Alder, B. J., "Cell Size Dependence of Transport Coefficient in Stochastic Particle Algorithms," *Physics of Fluids*, Vol. 10, No. 6, 1998, pp. 1540–1542.

[24]Alexander, F. J., Garcia, A. L., and, Alder, B. J., "Erratum: Cell Size Dependence of Transport Coefficient is Stochastic Particle Algorithms," *Physics of Fluids*, Vol. 12, No. 3, 2000, pp. 731–731.

[25]Guo, K. and Liaw, G.-S., "A Review: Boundary Conditions for the DSMC Method," in *35th AIAA Thermophysics Conference*, AIAA Paper 2001–2953, Anaheim, CA, June 11–14, 2001.

[26]Garcia, A. L., and, Wagner, W., "Time Step Truncation Error in Direct Simulation Monte Carlo," *Physics of Fluids*, Vol. 12, No. 10, 2000, pp. 2621–2633.

[27]Hadjiconstantinou, N. G., "Analysis of Discretization in the Direct Simulation Monte Carlo," *Physics of Fluids*, Vol. 12, No. 10, 2000, pp. 2634–2638.

[28]Santos, W. F. N., "Structure of the Shock Wave on Flat-Nose Power-Law Bodies," in *43nd AIAA Aerospace Sciences Meeting and Exhibit*, AIAA Paper 2005-0969, Reno, NV, January 10-13, 2005.